Core−Shell Nanocomposites Based on Gold Nanoparticle@Zinc−Iron-Embedded Porous Carbons Derived from Metal−Organic Frameworks as Efficient Dual Catalysts for Oxygen Reduction and Hydrogen Evolution Reactions

Jia Lu,[†] Weijia Zhou,*,[†] Likai Wang,[†] Jin Jia,[†] Yunting Ke,[†] Linjing Yang,[†] Kai Zhou,[†] Xiaojun Liu,[†] Zhenghua Tang,[†] Ligui Li,[†] and Shaowei Chen*,[†,‡]

[†]New Energy Research Institute, School of Environment and Energy, South China University of Technology, Guangzhou Higher Education Mega Center, Guangzhou, Guangdong 510006, China

[‡]Department of Chemistry and Biochemistry, University of California, 1156 High Street, Santa Cruz, California 95064, United States

Ⓢ *Supporting Information*

ABSTRACT: Core−shell nanocomposites based on Au nanoparticle@zinc−iron-embedded porous carbons (Au@Zn−Fe−C) derived from metal−organic frameworks were prepared as bifunctional electrocatalysts for both oxygen reduction reaction (ORR) and hydrogen evolution reaction (HER). A single Au nanoparticle of 50−100 nm in diameter was encapsulated within a porous carbon shell embedded with Zn−Fe compounds. The resulting Au@Zn−Fe−C hybrids exhibited apparent catalytic activity for ORR in 0.1 M KOH (with an onset potential of +0.94 V vs RHE, excellent stability and methanol tolerance) and for HER as well, which was evidenced by a low onset potential of −0.08 V vs RHE and a stable current density of 10 mA cm^{-2} at only −0.123 V vs RHE in 0.5 M H$_2$SO$_4$. The encapsulated Au nanoparticles played an important role in determining the electrocatalytic activity for ORR and HER by promoting electron transfer to the zinc−iron-embedded porous carbon layer, and the electrocatalytic activity was found to vary with both the loading of the gold nanoparticle cores and the thickness of the metal−carbon shells. The experimental results suggested that metal-embedded porous carbons derived from metal−organic frameworks might be viable alternative catalysts for both ORR and HER.

KEYWORDS: core−shell structure, metal−organic frameworks, oxygen reduction reaction, hydrogen evolution reaction, electron transfer
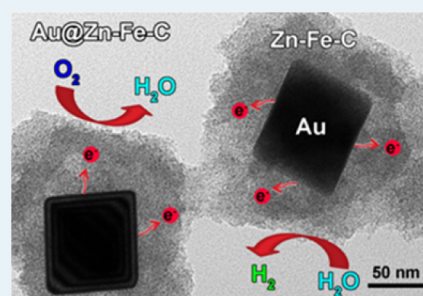
■ INTRODUCTION

Development of renewable and green energy sources has been attracting extensive research interest lately.[1] Of these methodologies, oxygen reduction reaction (ORR) has been found to play key roles in fuel cells and zinc-air batteries, while hydrogen evolution reaction (HER) is important in the production of clean and sustainable energy. Hence, the development of highly efficient electrocatalysts for both ORR and HER is crucial. Until now, platinum-based materials have been used extensively as the electrocatalysts of choice, because of their excellent catalytic activity toward ORR[2] and HER.[3,4] However, the low abundance and high price of platinum greatly limit their commercial applications.[5,6] Thus, development of cost-effective electrocatalysts with extraordinary ORR and HER activity is urgently needed. In fact, extensive research efforts have been devoted to the development of alternative materials that are low cost and naturally abundant that may eventually replace platinum-based catalysts. Toward this end, a variety of materials, including carbon nanostructures,[5,7−14] transition metals[6,15−18] and their oxides,[19−21] carbides,[22] and disulfides[23−25] have been prepared and examined as electrocatalysts

for ORR or HER. Nevertheless, it remains a key challenge to synthesize low-cost, highly active and stable catalysts for both ORR and HER.

Metal−organic frameworks (MOFs)—materials made of metal centers and functional organic ligands linked by coordination chemistry[26]—have been widely used in various fields, including gas storage/separation,[27−29] catalysis,[30−32] sensing,[33,34] and drug delivery.[35,36] MOFs have also been used as precursors and templates for the preparation of metal nanoparticles encapsulated in porous carbons with controlled morphologies, high surface area, and uniform porosity.[37−41] For instance, Hong et al.[40] synthesized nitrogen-doped porous carbon nanopolyhedra by simple carbonization of a zeolitic imidazolate framework (ZIF), which showed a remarkable performance for ORR, with an onset potential of −0.017 V vs Ag/AgCl, excellent methanol tolerance, and robust stability. In another study, Wu et al.[42] prepared porous molybdenum

carbide nano-octahedra via the calcination of a mixture of Cu-based MOFs and Mo-based precursors, which exhibited efficient electrocatalytic activity for hydrogen production in both acidic and alkaline solutions, with an overpotential of -0.142 V in 0.5 M H_2SO_4 and -0.151 V in 1 M KOH at a cathodic current density of 10 mA cm^{-2}. In these electrocatalysts, the significant improvement of the catalytic activity was attributed to the porous structure and exposure of active sites after calcination of the MOFs.

Indeed, metal−carbon composites have been widely employed as efficient electrocatalysts in alkaline solutions for ORR. However, for HER in acid solutions, the leaching of metals from the catalyst surface significantly decreases the electrocatalytic activity and stability. One effective strategy that will mitigate such a problem is to encapsulate metal nanoparticles into carbon nanotubes or carbon shells, to prevent the corrosion of the metal nanoparticles in acidic media, and, more importantly, to promote catalytic reactions on the carbon surface by electron transfer from the encapsulated metal nanoparticles.[6,43,44] Such core−shell structures can be readily prepared by calcination of MOFs at controlled temperatures, where MOFs are used as the metal and carbon sources. However, only a few studies have been reported so far in the literature where metal-embedded porous carbons derived from MOFs are used as HER catalysts in acid media.[1,42] In these studies, it has been argued that the formation of an core−shell structure is likely an effective strategy to produce hybrid catalysts with remarkable catalytic activity, as compared to single-component counterparts, because of the synergistic effects between the core and shell where the inside core may have an impact on the electron density of the outside shell.[45,46] For ORR, the core−shell structure may improve the performance and concurrently increase methanol tolerance and stability of the catalysts;[2,47,48] and for HER, the core−shell structure is anticipated to not only enhance the corrosion resistance of the metals in acidic electrolytes but also improve the HER activity via the synergistic contributions from both the core and shell.[49] Indeed, a variety of core−shell structures have been prepared and used for both ORR and HER catalysis, such as Au@Co$_3$O$_4$[50] and Co@N-doped carbon.[43] Note that, in these studies, the core metal nanoparticles alone exhibit only minimal catalytic activity; yet, the formation of a core−shell hybrid structure markedly enhances the catalytic performance of the outer shells. This is the primary motivation of the present study where gold nanoparticles are used as the cores that are coated with a porous carbon shell.

Herein, we prepared a multilevel core−shell structure of Au nanoparticle@zinc−iron-embedded porous carbons (Au@Zn−Fe−C) and used it as a bifunctional electrocatalyst for both ORR and HER. Experimentally, a single Au nanoparticle was wrapped by a porous carbon shell embedded with Zn−Fe compounds by using Zn−Fe-based MOFs as the metal and carbon sources. The structures of the core−shell Au@Zn−Fe−C hybrids were characterized by scanning electron microscopy (SEM), transmission electron microscopy (TEM), X-ray photoelectron spectroscopy (XPS), and X-ray diffraction (XRD) measurements. Electrochemical studies showed that Au@Zn−Fe−C exhibited an apparent electrocatalytic activity for both ORR in 0.1 M KOH and HER in 0.5 M H_2SO_4.

■ EXPERIMENTAL SECTION

Materials. All reagents were of analytical grade and used without further purification. Tetrachloroauric acid (HAuCl$_4$),

zinc nitrate hexahydrate (Zn(NO$_3$)$_2$·6H$_2$O), iron(III) acetylacetonate (Fe(acac)$_3$), 1,4-benzenedicarboxylic acid (H$_2$BDC), poly(vinylpyrrolidone) (PVP, molecular weight of 30 000), N,N-dimethylformamide (DMF), ethanol, 10 wt % Pt/C, and 20 wt % Pt/C were purchased from Sinopharm Chemical Reagents Beijing Co. Deionized water was supplied with a Barnstead Nanopure Water System (18.3 MΩ cm).

Synthesis of Fe,Zn-Embedded Porous Carbon Nanocomposites. In a typical reaction, 60 mg of Fe(acac)$_3$, 46.4 mg of Zn(NO$_3$)$_2$·6H$_2$O, and 9.6 mg of H$_2$BDC were dissolved in 25.6 mL of a DMF−ethanol (v:v = 5:3) mixed solution under magnetic stirring for 30 min. The resulting solution was transferred to a 40 mL Teflon-lined stainless-steel autoclave and then heated at 100 °C for 6 h in an oven before it was cooled to room temperature. The products were separated via centrifugation at 11 000 rpm for 15 min and further purified with DMF and ethanol several times. Subsequently, the products were dried at 80 °C for 24 h. The dried sample were placed in a tube furnace and heated at 600 °C for 2 h under an argon atmosphere at a heating rate of 2 °C min^{-1} (note that this temperature was determined by TGA measurements, because, at higher temperatures, the samples remained thermally stable (see Figure S1 in the Supporting Information)). The obtained powders were denoted as Zn−Fe−C. Porous carbons embedded with Zn only (denoted as Zn−C) were prepared using the same procedure but without the addition of Fe(acac)$_3$.

Synthesis of Au Nanoparticles. A quantity of 0.7284 g of PVP was dissolved in 8 mL of a DMF−ethanol (v:v = 5:3) mixed solution in a 15 mL autoclave. One hundred microliters (100 μL) of a HAuCl$_4$ solution that was pre-prepared by dissolving 1 g of HAuCl$_4$ in 40 mL of pure water was then added into the autoclave. The autoclave was transferred to an oven and heated at 140 °C for 3 h. After cooling to room temperature, the products were centrifuged and washed with ethanol several times before being redispersed in ethanol.

Synthesis of Au@Zn−Fe−C and Au@Zn−C Core−Shell Hybrids. To prepare Au@Zn−Fe−C, in a typical reaction, 0.2 g of PVP were dissolved in 23.6 mL of a DMF−ethanol (v:v = 5:3) mixed solution, into which was injected 1 mL of the Au nanoparticle solution obtained above under magnetic stirring for 30 min, where the final concentration of the Au nanoparticles was controlled at 0.17 M. Then, 60 mg of Fe(acac)$_3$, 46.4 mg of Zn(NO$_3$)$_2$·6H$_2$O, and 9.6 mg of H$_2$BDC were added into the above solution under magnetic stirring for another 30 min (corresponding to a Au:Fe molar ratio of 1:1). The resulting solution was transferred to a 40 mL Teflon-lined stainless-steel autoclave. The sealed vessel was then heated at 100 °C for 6 h before being cooled to room temperature. The products were separated via centrifugation at 11 000 rpm for 15 min and further purified with DMF and ethanol for several times. Subsequently, the product was dried at 80 °C for 24 h. The dried samples were placed in a tube furnace and heated at 600 °C for 2 h under an argon atmosphere at a heating rate of 2 °C min^{-1}. The obtained powders were denoted as Au@Zn−Fe−C. Au@Zn−C was prepared in a similar manner, but using Zn−C instead of Zn−Fe−C.

For comparison, composites were also synthesized by the same procedure but with the addition of a different amount of Au nanoparticles, which were denoted as Au@Zn−Fe−C-L, Au@Zn−Fe−C-H, in which the molar ratio of the Au and Fe precursors added in the synthesis process was 1:2 and 2:1, respectively.

Characterization. Field-emission scanning electron microscopy (FESEM) (Nova Nanosem 430, FEI) measurements were employed to characterize the morphologies of the as-prepared samples. Transmission electron microscopy (TEM) measurements were carried out with a Tecnai G220 FEI microscope. Powder X-ray diffraction (XRD) patterns of the samples were recorded on a powder X-ray diffractometer (Bruker, Model D8 Avance) with Cu Kα (λ = 0.15406 nm) radiation. X-ray photoelectron spectroscopy (XPS) measurements were performed (PHI, Model X-tool). Raman spectra were acquired on a Raman spectroscopy instrument (Renishaw invia) with an argon laser source of 488 nm in a macroscopic configuration. Nitrogen adsorption−desorption analysis was conducted with an ASAP 2020 instrument to evaluate the specific surface areas of the samples. Thermogravimetric analysis (TGA) analysis was also performed (Mettler Toledo, Model TGA/DSC 1).

Electrochemistry. Electrochemical measurements of ORR activity were performed with an electrochemical workstation (CH Instruments, Inc., Model CHI 750E) in a 0.1 M KOH aqueous solution. A rotating ring-disk electrode (RRDE) with a glassy carbon disk and gold ring was used as the working electrode. A Ag/AgCl electrode (3 M KCl) and a platinum foil were used as the reference and counter electrode, respectively. Four milligrams (4 mg) of the catalyst powders were dispersed in 1 mL of 1:4 (v:v) ethanol/water mixed solvents, along with 80 μL of a Nafion solution (5% Nafion in ethanol), and the mixture was sonicated for 30 min. Then, 10 μL of the above solution was dropcast onto the surface of the glassy carbon electrode (GCE) disk at a catalyst loading of 0.204 mg cm^{-2} and dried at room temperature. The polarization curves were acquired at 10 mV s^{-1} from 0 to −1.0 V (vs Ag/AgCl) at different electrode rotation rates (100−2500 rpm) in O$_2$-saturated 0.1 M KOH. CV tests were performed at 50 mV s^{-1} from 0 to −1.0 V (vs Ag/AgCl) in N$_2$ and O$_2$-saturated 0.1 M KOH. The numbers of electron transfer were calculated from RRDE data using the equation, $n = 4I_D/(I_D + I_R/N)$, where I_D and I_R are the disk current and the ring current, respectively, and N is the current collection efficiency (0.37) of the Au ring. Chronoamperometric measurements were performed at +0.47 V vs RHE for 30 000 s in O$_2$-saturated 0.1 M KOH.

HER measurements were also performed with the electrochemical workstation (CHI, Model 760C) but in a 0.5 M H$_2$SO$_4$ aqueous solution. A Hg/Hg$_2$Cl$_2$ electrode and a carbon rod were used as the reference and counter electrode, respectively. Four milligrams (4 mg) of the catalyst powders was dispersed in 1 mL of 4:1 (v:v) water/ethanol mixed solvents, along with 80 μL of a Nafion solution (5% Nafion in ethanol), and the mixture was sonicated for 30 min. Then, 5 μL of the above solution was drop-cast onto the surface of the glassy carbon disk (or carbon cloth) at a catalyst loading of 0.285 mg cm^{-2}. The as-prepared catalyst film was dried at room temperature. Polarization curves were acquired by sweeping electrode potentials from 0 to −0.8 V (vs Hg/Hg$_2$Cl$_2$) at a potential sweep rate of 5 mV s^{-1}. Accelerated stability tests were performed at room temperature by potential cycling between 0 and −0.5 V (vs Hg/Hg$_2$Cl$_2$) at a sweep rate of 100 mV s^{-1} for 1000 cycles. Current−time responses were monitored by chronoamperometric measurements at −0.15 V vs RHE for 12 h.

■ RESULTS AND DISCUSSION

The fabrication procedure of core−shell Au@Zn−Fe−C hydrids is depicted schematically in Figure 1a. The synthetic
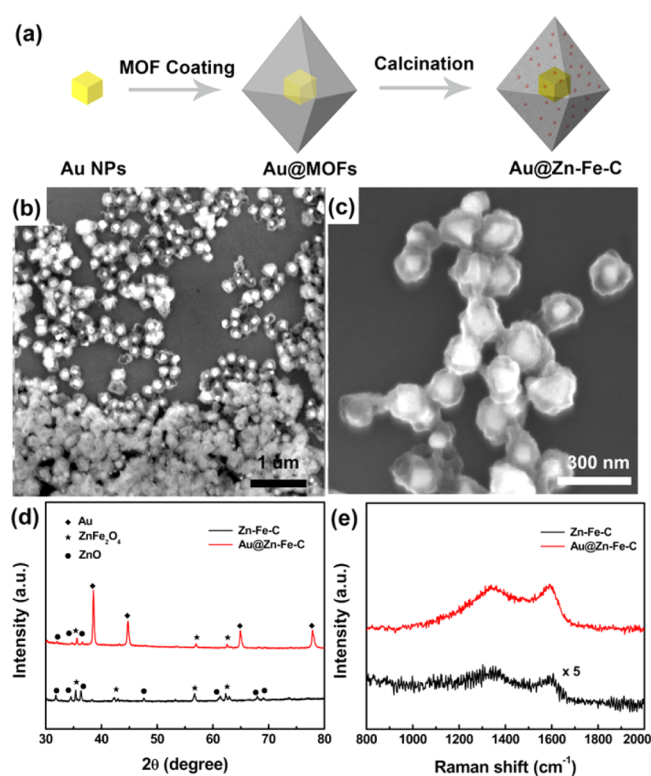

Figure 1. (a) Schematic illustration of the synthetic process of Au@Zn−Fe−C core−shell nanostructures. (b, c) Representative SEM images of Au@Zn−Fe−C, (d) XRD patterns, and (e) Raman spectra of Zn−Fe−C and Au@Zn−Fe−C hybrids.

process mainly included three steps: (i) Au nanoparticles were synthesized by chemical reduction of HAuCl$_4$; (ii) a Zn−Fe-MOF shell was grown on the nanoparticle surface, and (iii) the Zn−Fe-MOFs shell was converted to porous carbons embedded with zinc−iron compounds (Zn−Fe−C) through a simple calcination process. Experimentally, Au nanoparticles were prepared by reducing HAuCl$_4$ at 140 °C with DMF both as a solvent and as a reducing reagent in the presence of PVP which stabilized the Au nanoparticles; this procedure was described previously by Tang et al.[51] Then, a Zn−Fe-MOF shell was grown on the Au nanoparticle surface by using Fe(acac)$_3$ as the iron source, Zn(NO$_3$)$_2$ as the zinc source (and an activating reagent for pore formation), H$_2$BDC as organic linkers, and a DMF−ethanol mixed solution as the solvent. PVP was also added in the above mixture as a stabilizing reagent for the formation of a uniform Zn−Fe-MOF shell. Finally, the Zn−Fe-MOF shell was converted to porous carbons embedded with zinc−iron compounds by a simple calcination process in an argon atmosphere, forming core−shell Au@Zn−Fe−C hybrids.

SEM measurements were then carried out to confirm the successful preparation of Au@Zn−Fe−C core−shell nanostructures. From Figures 1b and 1c, we can see that Au@Zn−Fe−C inherited the octahedral structure of Zn−Fe-MOFs (Figure S2 in the Supporting Information),[52] although with a somewhat roughened surface, and the sample indeed exhibited a well-defined core−shell structure and a rather uniform size and shape. The crystal structures of Au@Zn−Fe−C were further investigated by XRD measurements. Figure 1d shows that a series of diffraction peaks emerged at 2θ = 38.2° for Au(111), 44.6° for Au(200), 64.6° for Au(220), and 77.8° for Au(311) (JCPDS File Card No. 001-1172); the peaks at 2θ =

35.6°, 43.1°, 56.9°, 62.7° are consistent with the (222), (400), (110), and (103) planes of ZnFe$_2$O$_4$ (JCPDS File Card No. 077-0011); and those at $2\theta = 32.0°$, 34.7°, and 36.5° arose from the (100), (002), and (101) diffractions of ZnO (JCPDS File Card No. 075-0576). Raman measurements of Zn−Fe−C and Au@Zn−Fe−C (Figure 1e) further confirm the structural composition, where the characteristic D and G bands of graphitic carbons can be seen at 1340 and 1589 cm^{-1} in both Zn−Fe−C and Au@Zn−Fe−C, which arose from the disordered C atoms and sp^2 hybridized graphitic C atoms, respectively.[53] With the encapsulation of Au nanoparticles, the intensities of the D and G bands in Au@Zn−Fe−C became much stronger than those of Zn−Fe−C (~10 times), likely due to the surface enhanced Raman scattering (SERS) effects of Au nanoparticles in the core;[54,55] and the ratio of the D and G band intensities (I_D/I_G) decreased slightly from 1.05 to 1.02, implying an increasing degree of graphitization of the carbon, although with abundant defects in both samples. The small variation of I_D/I_G also indicates that Fe and Zn, not the Au cores, played a dominant role in determining the graphitization (and defects) of the carbon shells.[56]

TEM measurements were then performed to further characterize the morphology and structure of the Au@Zn−Fe−C hybrids. Figure 2a shows a typical TEM image of Au@
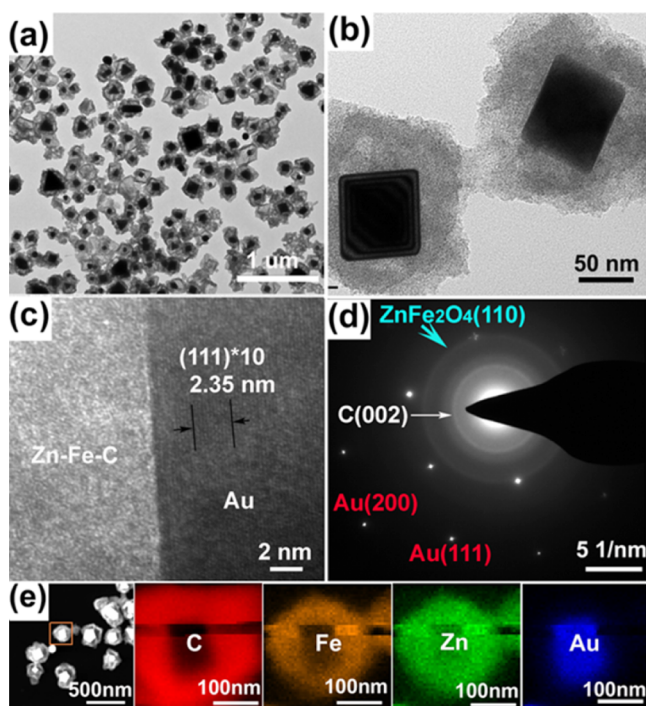

Figure 2. (a, b) Representative TEM, (c) HRTEM images, (d) the corresponding SAED patterns, and (e) EDX maps of Au@Zn−Fe−C hybrids.

Zn−Fe−C, which exhibited an average diameter of 214.5 nm (Figure S3 in the Supporting Information). At higher magnification (Figure 2b), one can clearly see a dark-contrast object of ~50−100 nm located at the center that was, most likely, a Au nanoparticle; and the Au nanoparticle was wrapped with a uniform, light-contrast Zn−Fe−C shell of 30−60 nm. Note that only short-range crystalline lattices can be observed in the Zn−Fe−C shell, whereas for the Au nanoparticle, one can see very well-defined lattice fringes with an interplanar

spacing of 0.235 nm that is in good agreement with the spacing of the (111) planes of face-centered cubic (fcc) Au (Figure 2c). Consistent behaviors were observed in selected area electron diffraction (SAED) measurements (Figure 2d), where the patterns suggested polycrystalline zinc−iron compounds, disordered carbon shells, and single-crystalline Au cores, as manifested by the scattered dots (Au) and diffraction rings (Zn−Fe−C). EDX mapping of a selected Au@Zn−Fe−C shows that the Au core was indeed surrounded by a uniform Zn−Fe-embedded porous carbon shell (Figure 2e). The BET surface area of Au@Zn−Fe−C was then quantified by nitrogen adsorption−desorption measurements, which was 8.7 m^2 g^{-1}, smaller than that (19.4 m^2 g^{-1}) of the Zn−Fe−C counterparts, because of the high mass density of the Au nanoparticles (Figure S4 in the Supporting Information).

XPS measurements were then carried out to investigate the chemical composition, as well as elemental valence states. The survey spectrum in Figure 3a confirmed the presence of C, Zn,
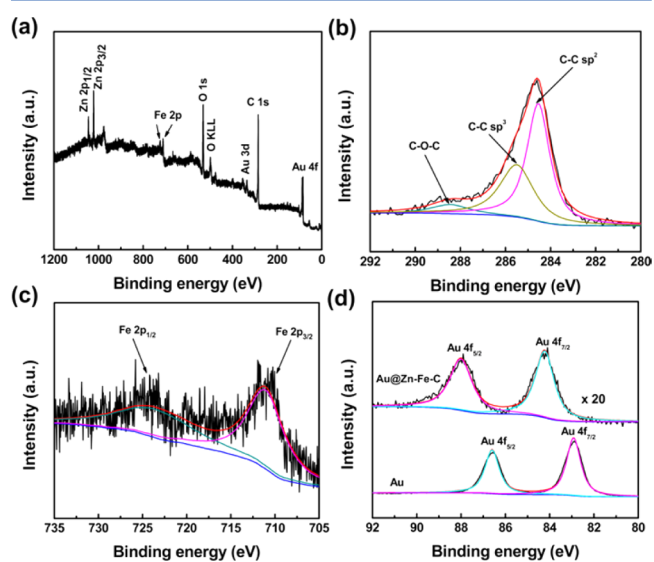

Figure 3. (a) XPS survey spectrum and high-resolution scans of (b) C 1s, (c) Fe 2p, and (d) Au 4f electrons of the Au@Zn−Fe−C hybrids. The spectrum of the Au 4f electrons of pure Au nanoparticles is also included in panel (d). Black curves are experimental data and colored curves are deconvolution fits.

Fe, and Au elements in Au@Zn−Fe−C. From the high-resolution scan in Figure 3b, the C 1s spectrum may be deconvoluted into three peaks, sp^2-hybridized graphite-like carbon (C=C) at 284.6 eV, sp^3-hybridized diamond-like carbon (C−C) at 285.5 eV, and C−O−C bond at 288.5 eV.[40] For Fe 2p electrons (Figure 3c), two distinct peaks can be identified at 711.3 and 724.5 eV, which can be assigned to the Fe 2p$_{3/2}$ and Fe 2p$_{1/2}$ electrons, respectively. In addition, the binding energies of Au 4f$_{7/2}$ and Au 4f$_{5/2}$ for Au@Zn−Fe−C (top curve, Figure 3d) can be identified at 84.2 and 88.0 eV, in comparison with those of pure Au nanoparticles (Au 4f$_{7/2}$ 82.8 eV and Au 4f$_{5/2}$ 86.6 eV, bottom curve). The positive shift of ca. 1.4 eV suggested that electron transfer likely occurred from the encapsulated Au nanoparticles into the Zn−Fe−C shell. Furthermore, on the basis of the integrated peak areas, the atomic contents of Au and Fe in Au@Zn−Fe−C were estimated to be 3.2 at. % and 5.9 at. %, respectively (see Table S1 in the Supporting Information).

The electrocatalytic activity of Au@Zn−Fe−C for ORR was then evaluated in an O_2-saturated 0.1 M KOH solution using RRDE voltammetry. The potentials were referenced to a reversible hydrogen electrode (RHE). Pure Au nanoparticles, Zn−Fe−C, and 10 wt % Pt/C were also tested as controls (note that Zn−Fe−C prepared by pyrolysis at temperatures higher than 600 °C did not show any apparent difference of the ORR performance; see Figure S5 in the Supporting Information). As shown in Figure 4a, Au@Zn−Fe−C (green
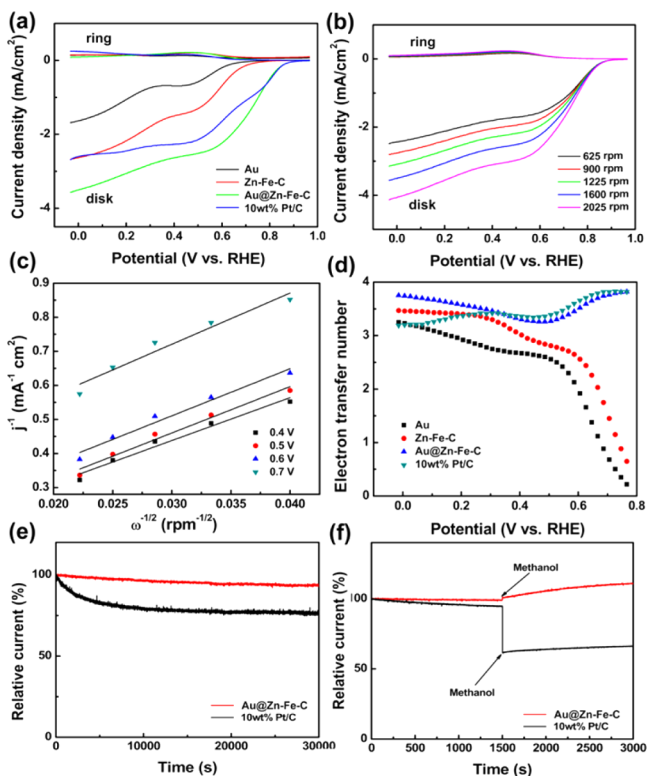

Figure 4. (a) RRDE voltammograms of Au nanoparticles, Zn−Fe−C, Au@Zn−Fe−C, and 10 wt % Pt/C at a rotation rate of 1600 rpm in an O_2-saturated 0.1 M KOH solution at 10 mV s^{-1}. (b) RRDE voltammograms of Au@Zn−Fe−C at different rotation rates in an O_2-saturated 0.1 M KOH solution at 10 mV s^{-1}. The ring potential was set at +1.5 V. (c) Koutecky−Levich plots of Au@Zn−Fe−C derived from RRDE data at different rotation rates in panel (b). (d) Number of electron transfer of Au nanoparticles, Zn−Fe−C, Au@Zn−Fe−C, and 10 wt % Pt/C, as a function of electrode potential. (e) Chronoamperometric responses of Au@Zn−Fe−C and 10 wt % Pt/C at +0.47 V vs RHE in an O_2-saturated 0.1 M KOH solution (900 rpm). (f) Chronoamperometric responses of Au@Zn−Fe−C and 10 wt % Pt/C at +0.466 V vs RHE in O_2-saturated 0.1 M KOH solution with the addition of 3 M methanol (900 rpm).

curve) showed an excellent electrocatalytic activity, with an onset potential of +0.94 V vs RHE, comparable to that of 10 wt % Pt/C (+0.94 V, blue curve), and a higher diffusion limited current density (2.63 mA cm^{-2} at +0.4 V) than that of 10 wt % Pt/C (2.27 mA cm^{-2}). Nevertheless, the ORR activity of Au@Zn−Fe−C was somewhat lower than that of 20 wt % Pt/C, which exhibited an onset potential at +1.01 V and a diffusion limited current density of 5.0 mA cm^{-2} at +0.4 V (Figure S6 in the Supporting Information). Cyclic voltammetric measurements of Au@Zn−Fe−C tested in O_2-saturated 0.1 M KOH also showed that apparent cathodic currents started to emerge at approximately +0.94 V (Figure S7 in the Supporting

Information). The fact that the onset potential of Au@Zn−Fe−C was markedly more positive than that of Zn−Fe−C (+0.84 V vs RHE, red curve) signifies the important role of the encapsulated Au nanoparticles in enhancing the ORR activity. However, pure Au nanoparticles (black curve, with a representative TEM image shown in Figure S8 in the Supporting Information) exhibited only a poor ORR performance with the onset potential at +0.80 V. These results imply a synergistic interaction between the Au core and the Zn−Fe−C shell that played a crucial role in enhancing the electrocatalytic activity of Au@Zn−Fe−C for ORR. In addition, to distinguish the roles of Zn and Fe in the catalytic reactions, we also prepared Zn−C and Au@Zn−C and examined their electrocatalytic activity. Voltammetric studies (Figure S9 in the Supporting Information) showed that the ORR activity of both samples was markedly lower than that of Au@Zn−Fe−C, implying that iron, not zinc, was responsible for promoting the ORR activity of carbon.

RRDE measurements were also conducted at different rotation rates to further investigate the electron-transfer kinetics of Au@Zn−Fe−C, and the results are shown in Figure 4b. The corresponding Koutecky−Levich (K-L) plots within the potential range of +0.4 V to +0.7 V are included in Figure 4c. The good linearity with a rather consistent slope of Au@Zn−Fe−C suggests first-order reaction kinetics for ORR, with respect to oxygen concentration in the solution. The difference in ORR performance is also obvious in the number of electron transfers (n) involved in ORR. As depicted in Figure 4d, the n values for Au@Zn−Fe−C were between 3.26 and 3.82 within the potential range of 0 to +0.8 V, signifying that ORR largely followed a four-electron pathway, similar to that of 10 wt % Pt/C (3.19 to 3.82). In contrast, the n values at both pure Au nanoparticles and Zn−Fe−C were significantly lower, at only 0.22−3.28 and 0.65−3.48, respectively. Significantly, the ORR activity of Au@Zn−Fe−C (onset potential +0.94 V vs RHE, n = 3.26−3.82) was better than or at least comparable to those of other catalysts derived from MOFs that have been reported in recent literature (see Table S2 in the Supporting Information), such as carbon polyhedra derived from ZIF-67 (onset potential of +0.86 V vs RHE, n = 3.7),[57] nitrogen-doped porous carbons derived from ZIF-7 (onset potential of +0.87 V vs RHE, n = 3.68−3.8),[58] and highly graphitized nitrogen-doped porous carbon nanopolyhrdra derived from ZIF-8 (onset potential of +0.95 V vs RHE, n = 3.8−3.9).[40]

The durability of Au@Zn−Fe−C was tested by chronoamperometric measurements at 900 rpm in an O_2-saturated 0.1 M KOH solution, as shown in Figure 4e. It can be seen that, in addition to a high activity, Au@Zn−Fe−C also exhibited robust stability. After continuous operation at +0.47 V for 30 000 s, ~93.4% of the current density was retained. In contrast, the current density of commercial 10 wt % Pt/C catalyst exhibited a sharp decrease, to 73.6%. It was worth mentioning that Au@Zn−Fe−C also exhibited greater methanol tolerance than commercial 10 wt % Pt/C catalysts (Figure 4f), which was important for practical applications. A sharp decrease in the current density was observed for the 10 wt % Pt/C catalyst upon the addition of 3 M methanol. In contrast, the current density of Au@Zn−Fe−C even increased slightly with the addition of 3 M methanol.

To examine the effects of gold contents on the ORR activity, two additional samples were prepared by the same procedure but at the Au/Fe molar ratios of 1:2 and 2:1 (as confirmed by XPS measurements; see Table S1), which were denoted as

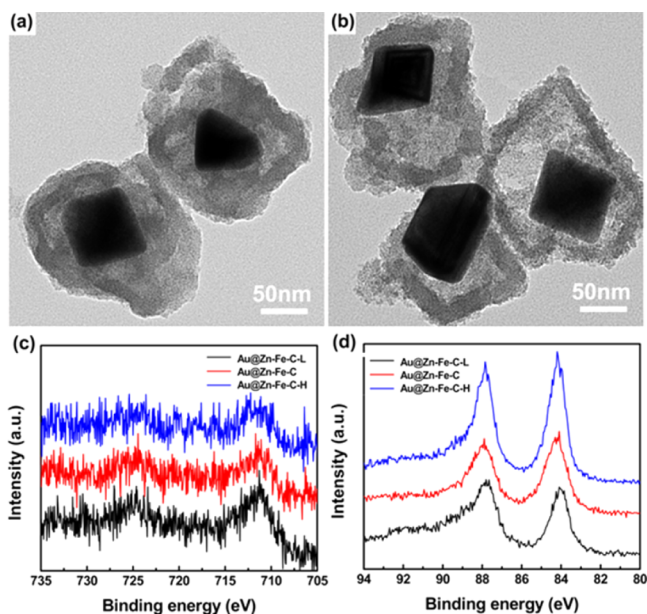Au@Zn−Fe−C-L and Au@Zn−Fe−C-H, respectively. From Figure 5, core−shell structures can be clearly seen in both

Figure 5. Representative TEM images of (a) Au@Zn−Fe−C-L (1:2) and (b) Au@Zn−Fe−C-H (2:1). High-resolution XPS scans of (c) Fe 2p and (d) Au 4f electrons of Au@Zn−Fe−C at different Au/Fe molar ratios.

samples, similar to Au@Zn−Fe−C (see Figure 2). However, one can see that the thickness of the Zn−Fe−C shells decreased as the Au/Fe molar ratios increased. Electrochemical studies were then carried out to assess and compare their ORR activity. From Figure S10 in the Supporting Information, it can be seen that Au@Zn−Fe−C-H showed a slightly lower ORR activity (onset potential of +0.92 V vs RHE) than Au@Zn−Fe−C. This may be ascribed to incomplete coating of the excessive Au nanoparticles by the carbon shells. Au@Zn−Fe−C-L also exhibited a more negative ORR onset potential (+0.86 V vs RHE) and a lower current density (1.38 mA cm^{-2} at +0.4 V) than Au@Zn−Fe−C. This is probably because of the limited contact between the Au nanoparticle and the carbon shell. That is, within the present experimental context, Au@Zn−Fe−C at the Au/Fe molar ratio of 1:1 represented the best catalysts for ORR among the series. Taken together, these results strongly suggest that the intimate electronic interactions between the Au core and the carbon shell played an important role in catalyzing the four-electron reduction of oxygen. Similar behaviors have been observed in the literature with, for instance, Au@Co$_3$O$_4$ for OER,[50] Fe@carbon nanotubes for ORR,[59] and CoNi@carbon for HER.[6]

The electrocatalytic activity of Au@Zn−Fe−C for HER was then investigated in 0.5 M H$_2$SO$_4$ in a three-electrode configuration. Figure 6a shows the polarization curves of the different samples in a 0.5 M H$_2$SO$_4$ aqueous solution. It can be seen that Au@Zn−Fe−C (blue curve) exhibited a low onset potential of −0.08 V vs RHE, which was much more positive than those for Au (−0.225 V, black curve) and Zn−Fe−C (−0.292 V, red curve) but slightly more negative than that of commercial 20 wt % Pt/C (−0.006 V, magenta curve) at the same catalyst loading. This suggests synergistic effects between the Au core and the Zn−Fe−C shell in enhancing the HER activity of Au@Zn−Fe−C. Moreover, at Au@Zn−Fe−C, an
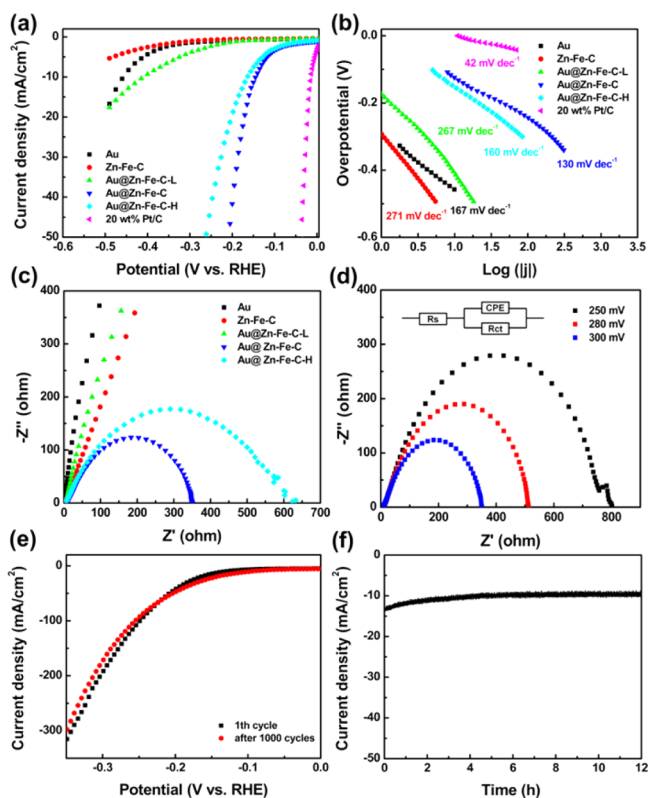

Figure 6. (a) Polarization curves and (b) corresponding Tafel plots of Au nanoparticles, Zn−Fe−C, Au@Zn−Fe−C-L, Au@Zn−Fe−C, Au@Zn−Fe−C-H, and 20 wt % Pt/C at 5 mV s^{-1} in a 0.5 M H$_2$SO$_4$ solution (iR-corrected). (c) Electrochemical impedance spectra of various samples for HER at −0.3 V. (d) Electrochemical impedance spectra of Au@Zn−Fe−C at various overpotentials for HER in 0.5 M H$_2$SO$_4$. Inset shows the equivalent circuit, where R_s is the (uncompensated) electrode series resistance, CPE is the constant-phase element, and R_{ct} is the charge-transfer resistance. (e) Polarization curves of Au@Zn−Fe−C before and after 1000 cycles in the stability test. (f) Time dependence of the HER current density of Au@Zn−Fe−C loaded on carbon cloth at −0.15 V vs RHE (iR-uncorrected).

overpotential of only −0.123 V was needed to reach a current density of 10 mA cm^{-2}. Just like tests conducted in ORR, the polarization curves of the Au@Zn−Fe−C samples at different Au/Fe molar ratios were also acquired to examine the impacts of the content of Au nanoparticles on the HER activity. It can be seen that the Au@Zn−Fe−C possessed the highest HER activity among all samples, suggesting that a proper thickness of the Zn−Fe−C shell was also important in enhancing the HER activity.

The Tafel slopes of the different samples were then compared (Figure 6b), which were obtained by fitting the linear portions of the polarization curves with the Tafel equation,

$$\eta = b \log j + a$$

where j is the current density and b is the Tafel slope. The Tafel slope of Au@Zn−Fe−C was 130 mV dec^{-1}, which was lower than those of other samples, for example, Au (167 mV dec^{-1}), Zn−Fe−C (271 mV dec^{-1}), Au@Zn−Fe−C-L (267 mV dec^{-1}), and Au@Zn−Fe−C-H (160 mV dec^{-1}), but much higher than that of the 20 wt % Pt/C (42 mV dec^{-1}). A lower Tafel slope corresponds to more favorable HER kinetics,

further confirming a synergistic contribution of the Au nanoparticle core and Zn−Fe−C shell. Mechanistically, there are three major reaction steps for HER in acidic electrolytes, including a primary discharge step (Volmer reaction, with a Tafel slope of 120 mV dec^{-1}) followed by an electrochemical desorption step (Heyrovsky reaction, with a Tafel slope of 40 mV dec^{-1}) or a recombination step of hydrogen adsorption on catalyst surfaces (Tafel reaction, with a Tafel slope of 30 mV dec^{-1}). The results obtained above indicate that HER at Au@Zn−Fe−C likely proceeded through a Volmer−Heyrovsky mechanism and the electrochemical discharge process was the rate-limiting step.

Note that such an HER performance of Au@Zn−Fe−C (onset potential −0.08 V vs RHE, −0.123 V vs RHE at 10 mA cm^{-2}, and Tafel slope of 130 mV dec^{-1}) was markedly better than or at least comparable to those of the most active HER electrocatalysts in acidic solutions that have been reported in recent literature (see Table S3 in the Supporting Information), for instance, nitrogen-doped graphene/Co-embedded porous carbon polyhedron hybrids derived from Co-MOFs (onset potential at −0.058 V vs RHE, −0.229 V vs RHE at 10 mA cm^{-2}, and Tafel slope of 126 mV dec^{-1}),[53] graphene oxide and copper-centered MOF composite (onset potential at −0.087 V vs RHE, and Tafel slope of 84 mV dec^{-1}),[1] porous molybdenum carbide nano-octahedra derived from MOFs (onset potential at −0.025 V vs RHE, −0.142 V vs RHE at 10 mA cm^{-2}, and Tafel slope of 53 mV dec^{-1}),[42] Co-embedded nitrogen-rich carbon nanotubes (onset potential at −0.05 V, −0.26 V vs RHE at 10 mA cm^{-2}, and Tafel slope of 69 mV dec^{-1}),[43] and FeCo-alloy into nitrogen-doped carbon nanotubes (onset potential at −0.07 V vs RHE, −0.275 V vs RHE at 10 mA cm^{-2}, and Tafel slope of 74 mV dec^{-1}).[60]

Electrochemical impedance spectroscopy (EIS) measurements were then carried out to further probe the electron-transfer kinetics involved. Figure 6c depicts the Nyquist plots acquired at −0.30 V for a GCE modified with the various catalyst samples. We can see that Au@Zn−Fe−C exhibited a smaller charge transfer resistance (R_{ct}) than other samples, as manifested by the smallest semicircle, consistent with the best HER performance. In addition, R_{ct} actually diminished markedly with increasing overpotential, from 792 Ω at −250 mV to 316 Ω at −300 mV, as depicted in Figure 6d.

In addition to excellent catalytic activity, Au@Zn−Fe−C also exhibited extraordinary HER stability in acid solution. Figure 6e depicts the polarization curves of Au@Zn−Fe−C before and after the stability tests, where a slight increase in the current can be observed after 1000 cycles of potential scans. Moreover, over 12 h of continuous operation at the applied potential of −0.15 V (vs RHE), the current density of Au@Zn−Fe−C loaded on carbon cloth remained virtually invariant, once again confirming the remarkable stability of Au@Zn−Fe−C for HER in 0.5 M H$_2$SO$_4$ solution (Figure 6f). Note that using carbon cloth as the working electrode minimized the accumulation of H$_2$ bubbles on the electrode surface during the stability test, as compared to the GCE (see Figure S11 in the Supporting Information).

Based on the above results and in conjunction with recent theoretical calculations of metal@carbon core−shell nanostructures, the remarkable bifunctional properties of Au@Zn−Fe−C might be ascribed to the encapsulation of Au nanoparticles within the Zn−Fe−C shell where effective electron transfer from the Au core to the Zn−Fe−C shell not only decreased the local work function of the carbon surface, but also changed the carbon electronic density of states (see, for instance, Figure 3d).

This resulted in the generation of new catalytically active sites on the carbon surface,[50] because the synergistic manipulation of the electronic structure of the porous carbons likely enhanced the adsorption of oxygen intermediates (in ORR) and protons (in HER). In fact, the unique advantage of a Au@Zn−Fe−C core−shell structure toward ORR and HER was also confirmed by the observation that a simple mixture of Au nanoparticles and Zn−Fe−C (denoted as Au/Zn−Fe−C) exhibited a much lower catalytic activity (Figure S12 in the Supporting Information). Interestingly, the electrocatalytic activity did not seem to be very sensitive to the core metals. For instance, when Pt@Zn−Fe−C was prepared in a similar fashion, the ORR and HER performances (Figure S13 in the Supporting Information) were actually similar to those of Au@Zn−Fe−C described above. Additional contributions might arise from the Zn−Fe compounds embedded within the porous carbons where the intimate electronic interactions between Zn−Fe and C have been found to also contribute to the composite catalytic activity.[53] Taken together, the remarkable features of high activity, favorable kinetics, and strong durability suggest that the strategy for the preparation of core−shell Au@Zn−Fe−C hybrids may be a viable route in the synthesis and engineering of effective multifunctional electrocatalysts for both ORR and HER.

■ SUMMARY

In the present study, multilevel core−shell Au@Zn−Fe−C hybrids were prepared by a facile pyrolysis procedure using metal−organic frameworks (MOFs) as functional precursors. The nanocomposite hybrids were synthesized by direct pyrolysis of a uniform Zn−Fe-MOF shell coated on a Au nanoparticle in an inert atmosphere, and they exhibited excellent electrocatalytic activities for oxygen reduction reaction (ORR) (a positive onset potential at +0.94 V vs RHE, excellent stability and methanol tolerance) and hydrogen reduction reaction (HER) (a low onset overpotential of −0.08 V and a stable current density of 10 mA cm^{-2} at −0.123 V in 0.5 M H$_2$SO$_4$). This was taken into account for the conducting shells of Zn−Fe−C for rapid electron transport and formation of active sites for electrocatalytic reactions promoted by the encapsulated Au nanoparticle, where the electrocatalytic activity was found to vary with both the loading of the Au nanoparticle cores and the thickness of the metal−carbon shells. These results may open up a new avenue for the rational design and engineering of core−shell hybrid structures based on metal nanoparticles and MOFs as multifunctional electrocatalysts for energy conversion applications.

■ ASSOCIATED CONTENT

Ⓢ Supporting Information
The Supporting Information is available free of charge on the ACS Publications website at DOI: 10.1021/acscatal.5b02302.

> Additional experimental data in Figures S1−S13 and Tables S1−S3 (PDF)

■ AUTHOR INFORMATION

Corresponding Authors
*E-mail: eszhouwj@scut.edu.cn (W. Zhou).
*E-mail: shaowei@ucsc.edu (S. Chen).
Notes
The authors declare no competing financial interest.

■ REFERENCES

(1) Jahan, M.; Liu, Z.; Loh, K. P. *Adv. Funct. Mater.* **2013**, *23*, 5363−5372.

(2) Xia, W.; Zou, R.; An, L.; Xia, D.; Guo, S. *Energy Environ. Sci.* **2015**, *8*, 568−576.

(3) Lukowski, M. A.; Daniel, A. S.; Meng, F.; Forticaux, A.; Li, L.; Jin, S. *J. Am. Chem. Soc.* **2013**, *135*, 10274−10277.

(4) Jiao, Y.; Zheng, Y.; Jaroniec, M.; Qiao, S. *Chem. Soc. Rev.* **2015**, *44*, 2060−2086.

(5) Yang, D.-S.; Bhattacharjya, D.; Inamdar, S.; Park, J.; Yu, J.-S. *J. Am. Chem. Soc.* **2012**, *134*, 16127−16130.

(6) Deng, J.; Ren, P.; Deng, D.; Bao, X. *Angew. Chem., Int. Ed.* **2015**, *54*, 2100−2104.

(7) Duan, J.; Chen, S.; Jaroniec, M.; Qiao, S. Z. *ACS Nano* **2015**, *9*, 931−940.

(8) Liu, X.; Zhou, Y.; Zhou, W.; Li, L.; Huang, S.; Chen, S. *Nanoscale* **2015**, *7*, 6136−6142.

(9) Liu, X.; Zhou, W.; Yang, L.; Li, L.; Zhang, Z.; Ke, Y.; Chen, S. *J. Mater. Chem. A* **2015**, *3*, 8840−8846.

(10) Zhou, K.; Zhou, W.; Liu, X.; Wang, Y.; Wan, J.; Chen, S. *ACS Appl. Mater. Interfaces* **2014**, *6*, 14911−14918.

(11) Ma, T. Y.; Ran, J.; Dai, S.; Jaroniec, M.; Qiao, S. Z. *Angew. Chem., Int. Ed.* **2015**, *54*, 4646−4650.

(12) Huang, J.; Hou, D.; Zhou, Y.; Zhou, W.; Li, G.; Tang, Z.; Li, L.; Chen, S. *J. Mater. Chem. A* **2015**, *3*, 22886−22891.

(13) Duan, J.; Chen, S.; Jaroniec, M.; Qiao, S. Z. *ACS Catal.* **2015**, *5*, 5207−5234.

(14) Zheng, Y.; Jiao, Y.; Qiao, S. Z. *Adv. Mater.* **2015**, *27*, 5372−5378.

(15) Zhou, M.; Yang, C.; Chan, K.-Y. *Adv. Energy Mater.* **2014**, *4*, 1400840.

(16) Zhou, W.; Zhou, Y.; Yang, L.; Huang, J.; Ke, Y.; Zhou, K.; Li, L.; Chen, S. *J. Mater. Chem. A* **2015**, *3*, 1915−1919.

(17) Hou, Y.; Wen, Z.; Cui, S.; Ci, S.; Mao, S.; Chen, J. *Adv. Funct. Mater.* **2015**, *25*, 872−882.

(18) Chen, S.; Duan, J.; Bian, P.; Tang, Y.; Zheng, R.; Qiao, S.-Z. *Adv. Energy Mater.* **2015**, *5*, 1500936.

(19) Cheng, F.; Su, Y.; Liang, J.; Tao, Z.; Chen, J. *Chem. Mater.* **2010**, *22*, 898−905.

(20) Zhang, C.; Antonietti, M.; Fellinger, T.-P. *Adv. Funct. Mater.* **2014**, *24*, 7655−7665.

(21) Duan, J.; Chen, S.; Dai, S.; Qiao, S. Z. *Adv. Funct. Mater.* **2014**, *24*, 2072−2078.

(22) Zhao, Y.; Kamiya, K.; Hashimoto, K.; Nakanishi, S. *J. Am. Chem. Soc.* **2015**, *137*, 110−113.

(23) Chen, S.; Duan, J.; Tang, Y.; Jin, B.; Zhang Qiao, S. *Nano Energy* **2015**, *11*, 11−18.

(24) Zhao, Y.; Kuai, L.; Liu, Y.; Wang, P.; Arandiyan, H.; Cao, S.; Zhang, J.; Li, F.; Wang, Q.; Geng, B.; Sun, H. *Sci. Rep.* **2015**, *5*, 8722.

(25) Duan, J.; Chen, S.; Chambers, B. A.; Andersson, G. G.; Qiao, S. Z. *Adv. Mater.* **2015**, *27*, 4234−4241.

(26) Li, X.; Guo, Z.; Xiao, C.; Goh, T. W.; Tesfagaber, D.; Huang, W. *ACS Catal.* **2014**, *4*, 3490−3497.

(27) Farha, O. K.; Özgür Yazaydın, A.; Eryazici, I.; Malliakas, C. D.; Hauser, B. G.; Kanatzidis, M. G.; Nguyen, S. T.; Snurr, R. Q.; Hupp, J. T. *Nat. Chem.* **2010**, *2*, 944−948.

(28) Rosi, N. L.; Eckert, J.; Eddaoudi, M.; Vodak, D. T.; Kim, J.; O'Keeffe, M.; Yaghi, O. M. *Science* **2003**, *300*, 1127−1129.

(29) Bae, T.-H.; Lee, J. S.; Qiu, W.; Koros, W. J.; Jones, C. W.; Nair, S. *Angew. Chem., Int. Ed.* **2010**, *49*, 9863−9866.

(30) Fu, Y.; Sun, D.; Chen, Y.; Huang, R.; Ding, Z.; Fu, X.; Li, Z. *Angew. Chem.* **2012**, *124*, 3420−3423.

(31) Li, B.; Leng, K.; Zhang, Y.; Dynes, J. J.; Wang, J.; Hu, Y.; Ma, D.; Shi, Z.; Zhu, L.; Zhang, D.; Sun, Y.; Chrzanowski, M.; Ma, S. *J. Am. Chem. Soc.* **2015**, *137*, 4243−4248.

(32) Zhang, L.; Shi, L.; Huang, L.; Zhang, J.; Gao, R.; Zhang, D. *ACS Catal.* **2014**, *4*, 1753−1763.

(33) Guo, Z.; Xu, H.; Su, S.; Cai, J.; Dang, S.; Xiang, S.; Qian, G.; Zhang, H.; O'Keeffe, M.; Chen, B. *Chem. Commun.* **2011**, *47*, 5551−5553.

(34) Chen, B.; Yang, Y.; Zapata, F.; Lin, G.; Qian, G.; Lobkovsky, E. B. *Adv. Mater.* **2007**, *19*, 1693−1696.

(35) Horcajada, P.; Chalati, T.; Serre, C.; Gillet, B.; Sebrie, C.; Baati, T.; Eubank, J. F.; Heurtaux, D.; Clayette, P.; Kreuz, C.; Chang, J.-S.; Hwang, Y. K.; Marsaud, V.; Bories, P.-N.; Cynober, L.; Gil, S.; Ferey, G.; Couvreur, P.; Gref, R. *Nat. Mater.* **2010**, *9*, 172−178.

(36) Taylor-Pashow, K. M. L.; Rocca, J. D.; Xie, Z.; Tran, S.; Lin, W. *J. Am. Chem. Soc.* **2009**, *131*, 14261−14263.

(37) Sun, J.-K.; Xu, Q. *Energy Environ. Sci.* **2014**, *7*, 2071−2100.

(38) Liu, B.; Shioyama, H.; Akita, T.; Xu, Q. *J. Am. Chem. Soc.* **2008**, *130*, 5390−5391.

(39) Hou, Y.; Li, J.; Wen, Z.; Cui, S.; Yuan, C.; Chen, J. *Nano Energy* **2015**, *12*, 1−8.

(40) Zhang, L.; Su, Z.; Jiang, F.; Yang, L.; Qian, J.; Zhou, Y.; Li, W.; Hong, M. *Nanoscale* **2014**, *6*, 6590−6602.

(41) Wang, X.; Zhou, J.; Fu, H.; Li, W.; Fan, X.; Xin, G.; Zheng, J.; Li, X. *J. Mater. Chem. A* **2014**, *2*, 14064−14070.

(42) Wu, H. B.; Xia, B. Y.; Yu, L.; Yu, X.-Y.; Lou, X. W. *Nat. Commun.* **2015**, *6*, 6512.

(43) Zou, X.; Huang, X.; Goswami, A.; Silva, R.; Sathe, B. R.; Mikmeková, E.; Asefa, T. *Angew. Chem.* **2014**, *126*, 4461−4465.

(44) Deng, D.; Yu, L.; Chen, X.; Wang, G.; Jin, L.; Pan, X.; Deng, J.; Sun, G.; Bao, X. *Angew. Chem.* **2013**, *125*, 389−393.

(45) Kim, D.; Lee, Y. W.; Lee, S. B.; Han, S. W. *Angew. Chem., Int. Ed.* **2012**, *51*, 159−163.

(46) Koenigsmann, C.; Santulli, A. C.; Gong, K.; Vukmirovic, M. B.; Zhou, W.-p.; Sutter, E.; Wong, S. S.; Adzic, R. R. *J. Am. Chem. Soc.* **2011**, *133*, 9783−9795.

(47) Hou, Y.; Huang, T.; Wen, Z.; Mao, S.; Cui, S.; Chen, J. *Adv. Energy Mater.* **2014**, *4*, 1400337.

(48) Xi, J.; Xia, Y.; Xu, Y.; Xiao, J.; Wang, S. *Chem. Commun.* **2015**, *51*, 10479−10482.

(49) Zhou, W.; Zhou, J.; Zhou, Y.; Lu, J.; Zhou, K.; Yang, L.; Tang, Z.; Li, L.; Chen, S. *Chem. Mater.* **2015**, *27*, 2026−2032.

(50) Zhuang, Z.; Sheng, W.; Yan, Y. *Adv. Mater.* **2014**, *26*, 3950−3955.

(51) He, L.; Liu, Y.; Liu, J.; Xiong, Y.; Zheng, J.; Liu, Y.; Tang, Z. *Angew. Chem., Int. Ed.* **2013**, *52*, 3741−3745.

(52) Zhang, Z.; Chen, Y.; Xu, X.; Zhang, J.; Xiang, G.; He, W.; Wang, X. *Angew. Chem., Int. Ed.* **2014**, *53*, 429−433.

(53) Hou, Y.; Wen, Z.; Cui, S.; Ci, S.; Mao, S.; Chen, J. *Adv. Funct. Mater.* **2015**, *25*, 872−882.

(54) Schedin, F.; Lidorikis, E.; Lombardo, A.; Kravets, V. G.; Geim, A. K.; Grigorenko, A. N.; Novoselov, K. S.; Ferrari, A. C. *ACS Nano* **2010**, *4*, 5617−5626.

(55) Lu, G.; Li, H.; Liusman, C.; Yin, Z.; Wu, S.; Zhang, H. *Chem. Sci.* **2011**, *2*, 1817−1821.

(56) Sun, L.; Tian, C.; Li, M.; Meng, X.; Wang, L.; Wang, R.; Yin, J.; Fu, H. *J. Mater. Chem. A* **2013**, *1*, 6462−6470.

(57) Xia, W.; Zhu, J.; Guo, W.; An, L.; Xia, D.; Zou, R. *J. Mater. Chem. A* **2014**, *2*, 11606−11613.

(58) Zhang, P.; Sun, F.; Xiang, Z.; Shen, Z.; Yun, J.; Cao, D. *Energy Environ. Sci.* **2014**, *7*, 442−450.

(59) Deng, D.; Yu, L.; Chen, X.; Wang, G.; Jin, L.; Pan, X.; Deng, J.; Sun, G.; Bao, X. *Angew. Chem., Int. Ed.* **2013**, *52*, 371−375.

(60) Deng, J.; Ren, P.; Deng, D.; Yu, L.; Yang, F.; Bao, X. *Energy Environ. Sci.* **2014**, *7*, 1919−1923.